

Article

Fluid Dynamics Investigation in a Cold Flow Model of Internal Recycle Quadruple Fluidized Bed Coal Pyrolyzer

Xuepu Cao , Haoran Yu, Jianying Wang ^{*}, Lilong Zhou and Yongqi Hu ^{*}

College of Chemical and Pharmaceutical, Hebei University of Science & Technology, Shijiazhuang 050018, China; caoxp@hebust.edu.cn (X.C.); 16631112297@163.com (H.Y.); lanruohe@126.com (L.Z.)

* Correspondence: jenneywjy@163.com (J.W.); yongqi_h@163.com (Y.H.)

Abstract: Internal recycle quadruple fluidized bed pyrolyzer (IR-QFBP) consists of a dual fluidized bed pyrolyzer and a dual fluidized bed combustor and is proposed in this work. It is a new kind of efficient fluidized bed with high pyrolysis and energy efficiency. IR-QFBP may attract extensive attention because of its compact structure. Cold hydrodynamic characteristics of IR-QFBP are the bases of modeling and designing for the hot one. To fully understand the hydrodynamic characteristics of IR-QFBP, a cold flow model on a laboratory scale was designed and set up; furthermore, the two-fluid model (TFM) based simulation was also carried out. The pressure profiles, fluidization states, velocity profiles, and circulation rates of a solid powder at different operation conditions in IR-QFBP were investigated. The results showed that the stable internal circulation of solid powder can be achieved in IR-QFBP. And different circulation characteristics can be obtained by adjusting the operating conditions.

Keywords: IR-QFBP; coupling of pyrolyzer and combustor; hydrodynamic characteristics; experimental model; computational fluid dynamics



Citation: Cao, X.; Yu, H.; Wang, J.; Zhou, L.; Hu, Y. Fluid Dynamics Investigation in a Cold Flow Model of Internal Recycle Quadruple Fluidized Bed Coal Pyrolyzer. *Processes* **2024**, *12*, 625. <https://doi.org/10.3390/pr12030625>

Academic Editor: Raymond Cecil Everson

Received: 22 December 2023

Revised: 7 March 2024

Accepted: 15 March 2024

Published: 21 March 2024



Copyright: © 2024 by the authors. Licensee MDPI, Basel, Switzerland. This article is an open access article distributed under the terms and conditions of the Creative Commons Attribution (CC BY) license (<https://creativecommons.org/licenses/by/4.0/>).

1. Introduction

Coal is an important energy resource in the world. And a large portion of coal in the world is low-rank coal [1,2]. Hence, advanced technologies for the efficient utilization of low-rank coal are urgently required. Coal pyrolysis has been considered as an attractive method of using this low-rank coal [2–5]. Thus, it was necessary to reduce the energy consumption of the coal pyrolysis process, which would be more beneficial for saving energy and reducing cost in the downstream industry.

A number of studies have been proposed in coal pyrolysis, such as the multi-generation technologies coupling pyrolysis with combustion developed by Zhejiang University, the MRF process of China Coal Science and Technology Group Limited Company, the DG technology of Dalian University of Technology, and others [2,6]. Most of the above studies have the problems of high energy consumption or low heating rates [2,6].

So far, the main types of pyrolysis reactors that have been developed include fixed bed [7–9], bubbling fluidized bed [10–12], circulating fluidized bed [13–15], entrained flow [16,17], etc. Among them, circulating fluidized bed shows technological and commercial superiority for coal pyrolysis due to short residence time, fast heat transfer, and fast separation of volatiles and char [18,19], although it has some disadvantages such as requiring more fuel conditioning and capital investment [20]. Inspired by the advantage of the circulating fluidized bed, the dual fluidized bed (DFB) conversion technologies are proposed, which have a characteristic of using two fluidized bed (FB) reactors that are interconnected with circulated heat carrier particles for higher heating rates [21–28]. Based on the DFB technology, quadruple fluidized bed (QFB) system regarded as a cost-effective method is proposed [29–32]. However, it still belongs to the external circulating system,

which may lead to an increase in the equipment costs and reduction in heat transfer efficiency to a certain extent. Thus, there is still room to improve the circulating fluidized bed coal pyrolysis technology.

In this work, an internal recycle quadruple fluidized bed pyrolyzer (IR-QFBP) was first proposed [20,33], and the scheme of IR-QFBP is shown in Figure 1. IR-QFBP is divided into two zones including a pyrolysis zone (two axisymmetric high-speed beds) and a combustion zone (two axisymmetric low-speed beds). The circulating powder transports the heat of combustion from the combustion reactor to the pyrolysis reactor to meet the required temperature of pyrolysis.

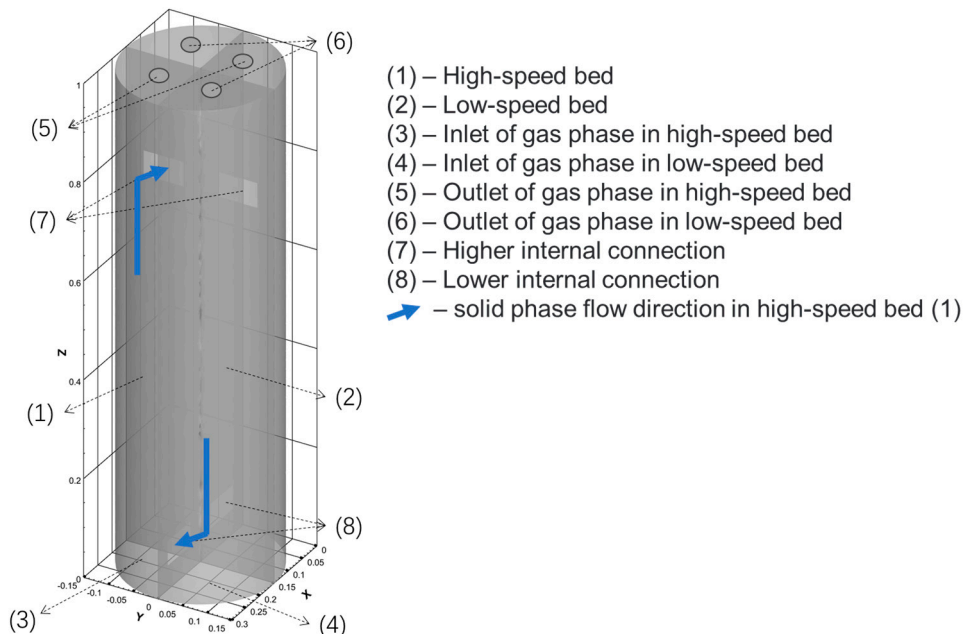


Figure 1. Scheme of IR-QFBP.

Hot coke powder is produced by air combustion with some coal powder in the low-speed bed, which enters the high-speed bed through the lower connection channel at the bottom and thus provides heat for the high-speed bed. The pulverized coal in the high-speed bed provides heat for the pyrolysis reaction. The pyrolyzed coal flows into the low-speed bed from the higher connection channel to form intra solid particle circulation and heat transfer. Coke powder as a product can be discharged from the bottom of the low-speed bed. The low-speed bed and the high-speed bed are separated by partitions, and only coke powder, at a high temperature, flows and generates heat exchange between the high-speed bed and the low-speed bed. The fluid flow direction of gas phase and solid phase in IR-QFBP is shown schematically in Figure 2. In the practical production, coal gas can be used as the carrier gas in the high-speed bed to avoid contact with air, which can improve the concentration of raw coal gas and reduce the subsequent separation cost. Oxygen or oxygen-enriched combustion is avoided in the low-speed bed, which can cancel the process of air separation process for oxygen production.

The problems for most of the previous studies on the industrial process of the utilization technology of low-rank pulverized coal are the serious waste of a large amount of sensible heat at high temperature, the inability to deal with a large amount of wastewater generated by ammonia water cooling [34,35], the bonding between the cooling tar and pulverized coal or coal ash, and the limited development of the tar-processing industry [36,37]. To solve these problems, we proposed a new idea for the utilization of low-rank pulverized coal, that is, coupling the low-order pulverized coal pyrolysis with the pyrolysis gas cracking in the subsequent operation.

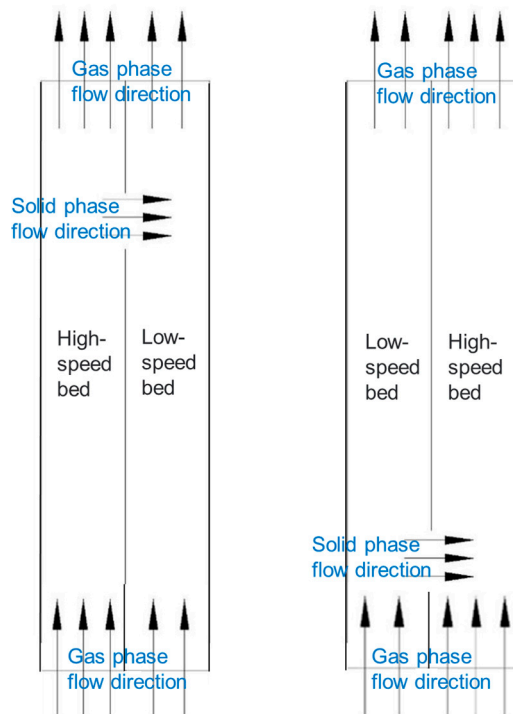


Figure 2. Schematic of the fluid flow direction in IR-QFBP.

The main content of the new idea is to pyrolyze low-rank pulverized coal through a coal pyrolysis reactor (IR-QFBP), and the pyrolysis products are the raw gas (gas and gaseous tar mixture at high temperature) and coke. Coke can be collected, sold, or used as a product. Raw gas is no longer cooled, but directly enters a high-temperature reactor (U-tube reactor), where the gaseous tar is directly decomposed into small molecules such as methane, CO, or H₂ through high-temperature cracking, partial oxidation, or steam reforming reactions. Small molecules can be burned for heating or participate in chemical reactions, which can maximize energy utilization efficiency.

The advantages of this new idea are summarized as follows: (1) the direct decomposition of the gaseous tar can produce H₂, which can provide sufficient raw materials for the hydrogen energy industry; (2) the post-treatment process of raw gas abandons the traditional ammonia water cooling process and no longer produces phenol-containing wastewater, which can reduce the cost of the treatment of phenol-containing wastewater by chemical enterprises; (3) the direct high-temperature reaction of the raw gas can make the full use of sensible heat in the raw gas, which improves the energy utilization efficiency; and (4) the tar in the coal gas is directly cracked, and thus, the tar and dust does not bond to cause pipeline obstruction.

In this idea, IR-QFBP is used as the low-rank pulverized coal pyrolysis reactor, and the U-tube reactor is used as the tar pyrolysis reactor. As the IR-QFBP is the key equipment in the whole process, we mainly focused on the characteristics of IR-QFBP in this work. The cold flow models under ambient conditions are widely applied to study the fluid dynamics for a new system [29,38–40]. And the hydrodynamic characteristics of IR-QFBP system are the bases of modeling and designing of a hot reactor. To fully understand the hydrodynamic characteristics, a cold flow model of IR-QFBP system on a laboratory scale was designed and set up in this work. The aluminum oxide particles were used as the solid materials. Meanwhile, the numerical model for IR-QFBP system was also established. Based on the experimental and numerical methods, the characteristics of fluidization state in IR-QFBP can be obtained. The effects of fluidization velocity on the volume fraction of solid phase, pressure profiles, and solid circulation rate were investigated. In order to verify the possibility of the pilot system of IR-QFBP, the hydrodynamic characteristics of the system were explored in this work, thus providing some ideas for reactor design.

2. Experiments

2.1. IR-QFBP Apparatus

As shown in Figure 3, the designed IR-QFBP for the experimental investigation is cylindrical in shape, and it is divided into three regions from the bottom to the top: the gas supply region, the reaction region, and the exhaust region. The gas supply region mainly includes four gas supply pipelines and a gas buffer chamber. The inner diameter of the air supply pipe is 45 mm, and the air is introduced from the side of the gas buffer chamber. The diameter and the height of the gas buffer chamber are 300 mm and 200 mm, respectively, and the gas buffer chamber is divided into four disconnected areas by the gas chamber cross baffle. A gas distributor is designed at the connection between the top of the gas buffer chamber and the bottom of the reaction region, and the gas distributor has been made with small holes with a diameter of 2 mm, as shown in the detailed drawing of Figure 3. The bubble cap distributor was used in our work, which can guarantee that the gas distributes uniformly when the equipment is operating, and the solid materials do not leak when the equipment shuts down. The diameter of the reaction region is 300 mm, the height is 1000 mm, and the thickness of the outer wall is 5 mm. The whole body is made of transparent plexiglass, and the copper wire mesh is set close to the inner wall of the plexiglass tube, which can remove static electricity. The interior of the reaction region is divided into four parts by a cross baffle, corresponding to the four parts of the gas buffer chamber. The reaction zone is divided into two high-speed bed zones and two low-speed bed zones. The two high-speed bed zones are centrally symmetrical, and the two low-speed bed zones are also centrally symmetrical. The connecting holes between the high-speed beds and low-speed beds are 80 mm long and 50 mm high and arranged at upper and lower intervals in a clockwise order. The exhaust region is composed of four plexiglass tubes with a diameter of 45 mm, which correspond to the four reaction areas. Four pressure-monitoring points are set at the top ($z = 0.9$ m) of the two high-speed beds and two low-speed beds, respectively. U-tube differential pressure gauges are used to measure the pressure difference between the high-speed bed and low-speed bed in this work. The main dimensions of IR-QFBP are summarized in Table 1.

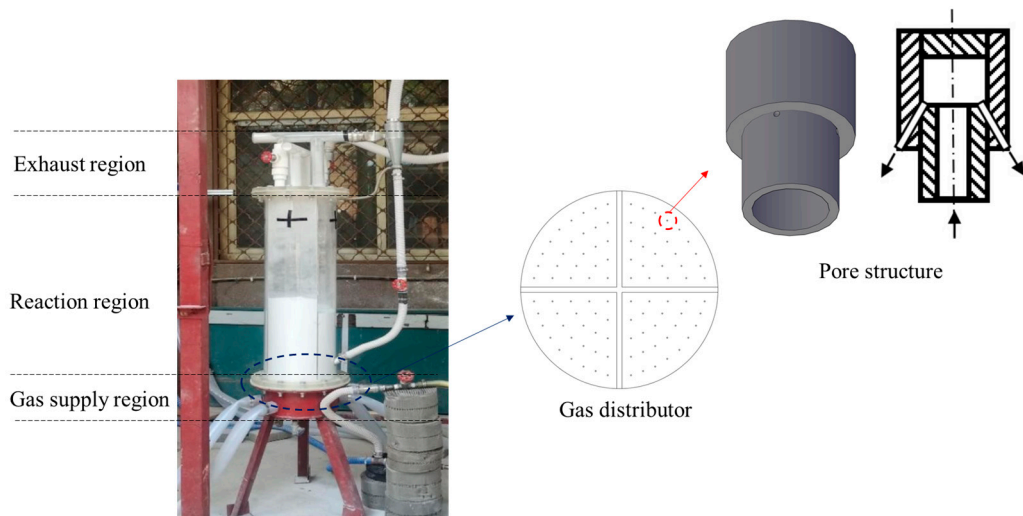


Figure 3. The experimental setup of IR-QFBP.

Table 1. Dimensions of IR-QFBP.

Parameter	Value
Height of the reaction region of IR-QFBP (H, mm)	1000
Diameter of IR-QFBP (D, mm)	300
Diameter of the gas outlet (mm)	45
Number of the gas outlets	4
Diameter of the hole in the inlet gas distributor (mm)	2
Number of the holes in the inlet gas distributor	100
Length of the internal connection (L_c , mm)	80
Width of the internal connection (W_c , mm)	50
Number of connections	4

2.2. Materials

Aluminum oxide particles are used as solid materials in IR-QFBP as it shows low toxicity, easy observation, and the similar physical properties of the low-rank pulverized coal, as shown in Table 2.

Table 2. Comparison of particle properties of aluminum oxide particles and low-rank pulverized coal.

Parameter	Aluminum Oxide	Low-Grade Pulverized Coal
Particle size (μm)	60 (average)	10~70
Particle density (kg/m^3)	3660	1900~2900
Specific surface area (m^2/g)	5000	800~19,500

2.3. Methodology

All the four parts of the reaction region of IR-QFBP are filled with aluminum oxide particles before the beginning of the experiment. The fluidization air for the four parts of the reaction region of IR-QFBP are supplied by four air compressors, respectively. During the experiment, the inlet velocity of high-speed beds and low-speed beds are varied, which can be adjusted by the air compressors.

In order to determine the inlet velocity of high-speed beds and low-speed beds, the minimum fluidization velocity of the aluminum oxide particles shown in Table 2 should be measured firstly. For this purpose, a pilot device was built, which mainly included a lifting tube, a gas chamber, a gas distributor, an air compressor, a buffer tank, and a U-tube differential pressure gauge. A plexiglass tube with a height of 3 m and an inner diameter of 30 mm is used as the lifting tube. A gas chamber is installed at the lower part of the lifting tube. A breathable sintering plate is used as the gas distributor. Flange connection is adopted to connect the above parts. The air compressor is connected to the buffer tank to supply the gas required for fluidizing the particles. The U-tube differential pressure gauge is connected to the lower part of the lifting tube to measure the pressure difference between the system and the outside. The minimum fluidization velocity was measured by the velocity-increasing method and the velocity-decreasing method at the same time. The steps of the measure experiment can be found in the reference of Kunii and Levenspiel [41].

Based on the minimum fluidization velocity obtained from the above methods, the inlet velocity of high-speed beds and low-speed beds can be roughly determined, which are usually several times larger than the minimum fluidization velocity [29].

3. Simulations

3.1. Physical Model

The hydrodynamics for the gaseous and liquid phases in IR-QFBP was simulated. The reaction region of IR-QFBP shown in Figure 1 was mainly investigated. The detailed geometry and fluid physical parameters used in this simulation are summarized in Tables 1 and 2, respectively.

3.2. Numerical Model

In this study, the computational simulations are performed by KTGF (Kinetic Theory of Granular Flow)-based Euler–Euler TFM (two-fluid model) approaches. It is assumed that the aluminum oxide powder is composed of spherical particles with same size and density as shown in Table 2. The temperatures of the air and particles are constant in the absence of chemical reactions, suggesting that both equations of energy conservation are neglected for simplicity. The inter-phase momentum exchange between gas and solid phases is calculated using the Gidaspow gas–solid drag model [42]. The governing equations and constitutive relations used in this study are summarized in Table 3 [43]. The subscripts f and s represent the gas and the solid phases, respectively. More details about the model can be found in the Fluent 16 manual.

Table 3. Governing equations and constitutive laws of TFM simulations.

Continuity equations	
$\frac{\partial}{\partial t}(\alpha_f \rho_f) + \nabla \bullet (\alpha_f \rho_f \mathbf{u}_f) = 0$	(1)
$\frac{\partial}{\partial t}(\alpha_s \rho_s) + \nabla \bullet (\alpha_s \rho_s \mathbf{u}_s) = 0$	(2)
Momentum equations	
$\frac{\partial}{\partial t}(\alpha_f \rho_f \mathbf{u}_f) + \nabla \bullet (\alpha_f \rho_f \mathbf{u}_f \mathbf{u}_f) = -\alpha_f \nabla p + \alpha_f \rho_f g + \nabla \bullet \alpha_f \boldsymbol{\tau}_f - \beta(\mathbf{u}_f - \mathbf{u}_s)$	(3)
$\frac{\partial}{\partial t}(\alpha_s \rho_s \mathbf{u}_s) + \nabla \bullet (\alpha_s \rho_s \mathbf{u}_s \mathbf{u}_s) = -\alpha_s \nabla p - \nabla p_s + \alpha_s \rho_s g - \nabla \bullet (\alpha_s \boldsymbol{\tau}_s) + \beta(\mathbf{u}_f - \mathbf{u}_s)$	(4)
where	
$\boldsymbol{\tau}_f = \mu_f [\nabla \mathbf{u}_f + (\nabla \mathbf{u}_f)^T] - \frac{2}{3} \mu_f (\nabla \bullet \mathbf{u}_f) \mathbf{I}$	(5)
$\boldsymbol{\tau}_s = \mu_s [\nabla \mathbf{u}_s + (\nabla \mathbf{u}_s)^T] + (\lambda_s - \frac{2}{3} \mu_s) (\nabla \bullet \mathbf{u}_s) \mathbf{I}$	(6)
Solid pressure	
$p_s = \alpha_s \rho_s \theta_s + 2 \rho_s (1+e) \alpha_s^2 g_0 \theta_s$	(7)
Solid phase bulk viscosity	
$\lambda_s = \frac{4}{3} \alpha_s 2 \rho_s d_s g_0 (1+e) \sqrt{\frac{\theta_s}{\pi}}$	(8)
Solid phase shear viscosity	
$\mu_s = \mu_{s,col} + \mu_{s,kin} + \mu_{s,fr}$	(9)
$\mu_{s,col} = \frac{4}{3} \alpha_s^2 \rho_s d_s g_0 (1+e) \sqrt{\frac{\theta_s}{\pi}}$	(10)
$\mu_{s,kin} = \frac{10 \rho_s d_s \sqrt{\theta_s \pi}}{96(1+e)g_0} \left[1 + \frac{4}{5} g_0 \alpha_s (1+e) \right]^2$	(11)
$\mu_{s,fr} = \frac{P_{s,friction} \sin \phi}{2 \sqrt{I_{2D}}}$	(12)
$P_{s,friction} = \begin{cases} 0 & \alpha_s < \alpha_{s,min} \\ 0.05 \frac{(\alpha_s - \alpha_{s,min})^2}{(\alpha_{s,max} - \alpha_s)^3} & \alpha_s \geq \alpha_{s,min} \end{cases}$	(13)
Radial distribution function	
$g_0 = \frac{3}{5} \left[1 - \left(\frac{\alpha_s}{\alpha_{s,max}} \right)^{\frac{1}{3}} \right]^{-1}$	(14)
Granular temperature equations	
$\frac{3}{2} \left[\frac{\partial(\alpha_s \rho_s \theta_s)}{\partial t} + \nabla \bullet (\alpha_s \rho_s \mathbf{u}_s \theta_s) \right] = (-p_s \mathbf{I} + \alpha_s \boldsymbol{\tau}_s) : \nabla \mathbf{u}_s + \nabla \bullet (k_s \nabla \theta_s) - \gamma - 3K_{gs} \theta_s$	(15)
Conductivity of fluctuating energy	
$k_s = \frac{150 \rho_s d_s \sqrt{\theta_s \pi}}{384(1+e)g_0} \left[1 + \frac{5}{6} g_0 \alpha_s (1+e) \right]^2 + 2 \alpha_s^2 \rho_s d_s g_0 (1+e) \sqrt{\frac{\theta_s}{\pi}}$	(16)
Collisional energy dissipation	
$\gamma = \frac{12(1-e^2)g_0}{d_s \sqrt{\pi}} \alpha_s^2 \rho_s \theta_s^{1.5}$	(17)
Inter-phase drag coefficient Gidaspow drag model	
$\beta = \begin{cases} 150 \left(\alpha_s^2 \mu_s / \alpha_f d_s^2 \right) + 1.75 \left[\rho_f \alpha_s \mathbf{u}_f - \mathbf{u}_s / d_s \right] & \alpha_f < 0.8 \\ \frac{3}{4} C_D \alpha_f - 2.65 \left[\rho_f \alpha_f \alpha_s \mathbf{u}_f - \mathbf{u}_s / d_s \right] & \alpha_f \geq 0.8 \end{cases}$	(18)
$C_D = \begin{cases} 24 / \left(Re \alpha_f \right) \left[1 + 0.15 \left(Re \alpha_f \right)^{0.687} \right] & Re < 1000 \\ 0.44 & Re \geq 1000 \end{cases}$	(19)

3.3. Simulation Settings

ANSYS Fluent 16 commercial package was used to model the gas–solid flow phenomena in IR-QFBP. The Pressure-Based type solver was used to solve the hydrodynamics equations. The computational domain was divided into about 130,000 cells. The calculation was performed on an HP workstation with 24 parallel 2.40 GHz Intel Xeon Silver 4214R processors.

The velocity inlet boundary condition was applied to the bottom boundary of the computational domain as a uniform velocity profile with $u_{f,z} = 0.1$ m/s for the high-speed beds and $u_{f,z} = 0.04$ m/s, 0.06 m/s, and 0.08 m/s for the low-speed beds. At the outlet boundary, the pressure outlet boundary condition was applied. The no slip conditions were set on the walls. The transient model was selected, and the time step was set as 0.001 s.

4. Results and Discussion

4.1. Minimum Fluidization Velocity

As shown in Figure 4, the curves measured by the velocity-increasing method and the velocity-decreasing method are not same, and the former in the range of pressure drop is greater than the opposite process. This is because when the fixed bed is converted to the fluidized bed, additional energy must be supplied to break the cohesion forces between the particles, and thus, the pressure drop peak is formed at the moment of flush out. However, the conclusion can be drawn that the minimum fluidization velocity is about 0.01 m/s from these two methods.

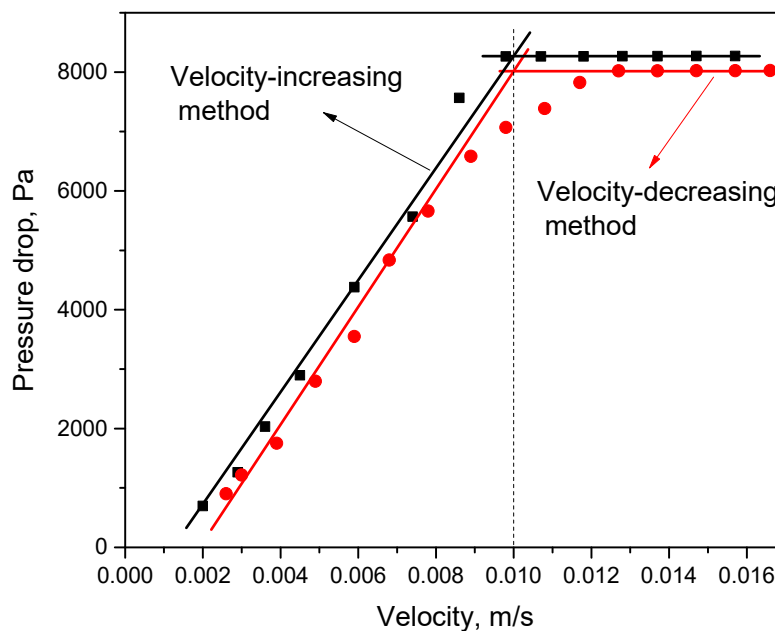


Figure 4. Relationship between pressure drop and fluidization velocity by velocity-increasing method and velocity-decreasing method.

4.2. Pressure Profiles

The pressure profile can vividly show the operation condition of the fluidized bed. Thus, the inner pressure profile in IR-QFBP was first investigated. The simulated pressure profiles when the fluid flow is fully developed with the inlet velocity of 0.1 m/s in high-speed beds and 0.04 m/s, 0.06 m/s, and 0.08 m/s in low-speed beds are shown in Figures 5–7.

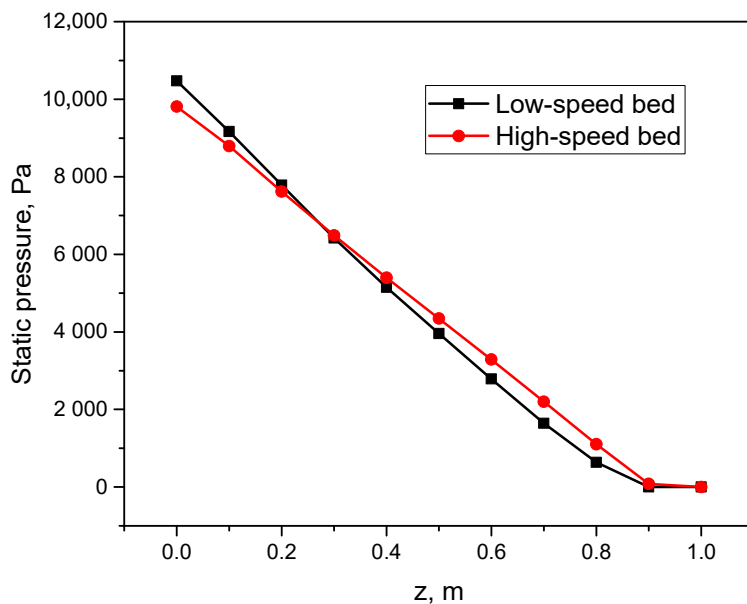


Figure 5. The pressure profiles with the inlet velocity of 0.1 m/s in high-speed beds and 0.04 m/s in low-speed beds.

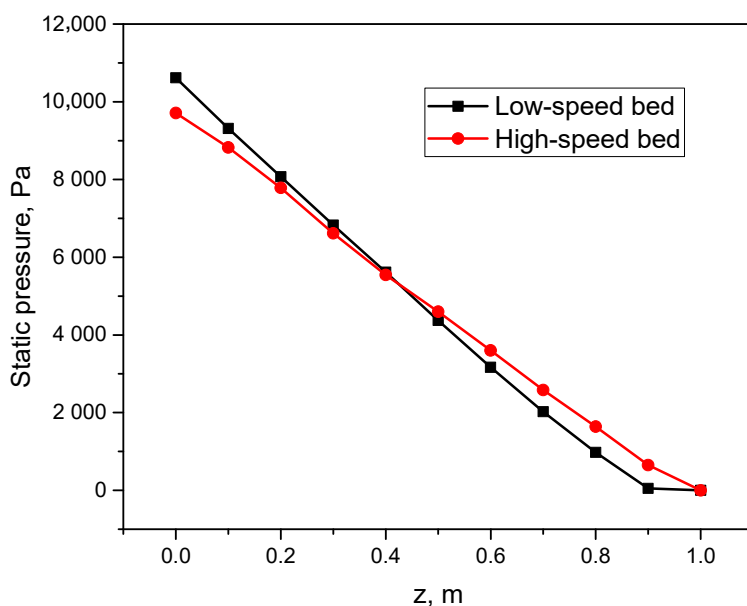


Figure 6. The pressure profiles with the inlet velocity of 0.1 m/s in high-speed beds and 0.06 m/s in low-speed beds.

The pressure profiles with the inlet velocity of 0.1 m/s in high-speed beds and 0.04 m/s in low-speed beds are shown in Figure 5. Both the pressures in the high-speed bed and in the low-speed bed are reduced with the increase in the height along z . The pressure in the high-speed bed is lower than that in the low-speed bed at $0 \text{ m} < z < 0.3 \text{ m}$, while, the pressure in the high-speed bed is higher than that in the low-speed bed at $0.3 \text{ m} < z < 0.9 \text{ m}$, which can maintain the fluid flow from the low-speed bed to the high-speed bed through the lower connection hole and from the high-speed bed to the low-speed bed through the higher connection hole.

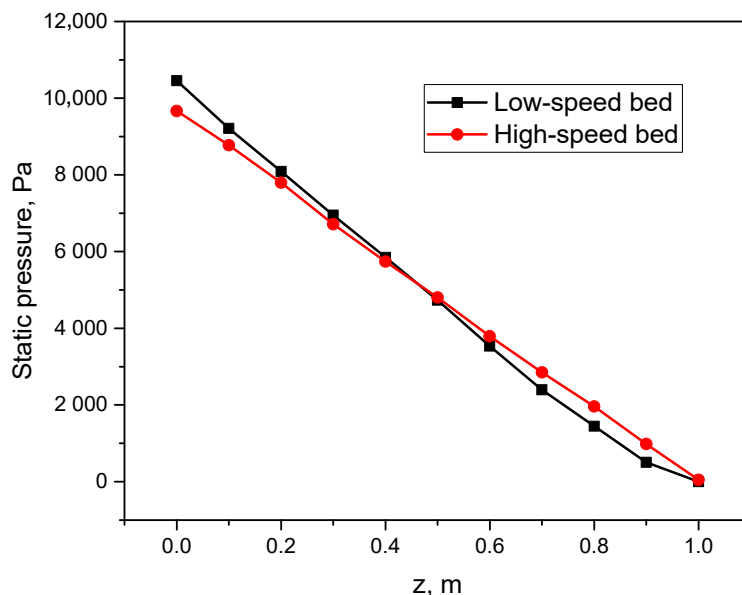


Figure 7. The pressure profiles with the inlet velocity of 0.1 m/s in high-speed beds and 0.08 m/s in low-speed beds.

The pressure profiles with the inlet velocity of 0.1 m/s in high-speed beds and 0.06 m/s in low-speed beds are shown in Figure 6. Same as the results in Figure 5, the pressures in the high-speed bed and in the low-speed bed are also reduced with the increase in the height along z . The pressure in the high-speed bed is lower than that in the low-speed bed at $0 \text{ m} < z < 0.4 \text{ m}$, while the pressure in the high-speed bed is higher than that in the low-speed bed at $0.4 \text{ m} < z < 1.0 \text{ m}$, which also maintain the stable internal circulation of solid materials in IR-QFBP.

The pressure profiles with the inlet velocity of 0.1 m/s in high-speed beds and 0.08 m/s in low-speed beds are shown in Figure 7. Same as the results in Figures 5 and 6, the pressures in the high-speed bed and in the low-speed bed are reduced with the increase in the height along z . The pressure in the high-speed bed is lower than that in the low-speed bed at $0 \text{ m} < z < 0.5 \text{ m}$, while the pressure in the high-speed bed is higher than that in the low-speed bed at $0.5 \text{ m} < z < 1.0 \text{ m}$, which also maintain the stable internal circulation of solid materials.

By comparing these three figures, the pressure differences between the high-speed bed and the low-speed bed in Figure 6 are larger than those in Figures 5 and 7, which may generate greater driving force for the internal circulation. Therefore, the operation conditions with the inlet velocity of 0.1 m/s in high-speed beds and 0.06 m/s in low-speed beds were mainly investigated in the following study.

The experimental pressure differences between the high-speed bed and the low-speed bed can be measured through the method shown in Section 2.1. The simulated pressure differences at $z = 0.9 \text{ m}$ were selected, as the pressure-monitoring points were set near this location of the apparatus. The results for the three cases are summarized in Table 4. As can be seen, the simulated values are close to the experimental values, which can verify the accuracy of the simulation model used in our work.

The pressure profiles with the inlet velocity of 0.1 m/s in high-speed beds and 0.06 m/s in low-speed beds at different times are shown in Figure 8. At the beginning of fluidization, the pressures in the high-speed bed and in the low-speed bed are almost the same. As the fluidization proceeds, pressure differences between the high-speed bed and the low-speed bed begin to appear. When the pressure differences are almost constant, fluidization is considered to be fully developed, and the time of which is about 16 s.

Table 4. Simulated and experimental results comparison of pressure differences between the high-speed bed and the low-speed bed.

	Inlet Velocity of High-Speed Bed (m/s)	Inlet Velocity of Low-Speed Bed (m/s)	Simulated Pressure Differences (Pa)	Experimental Pressure Differences (Pa)
Case 1	0.1	0.04	467.5	460
Case 2	0.1	0.06	662.2	660
Case 3	0.1	0.08	518.3	520

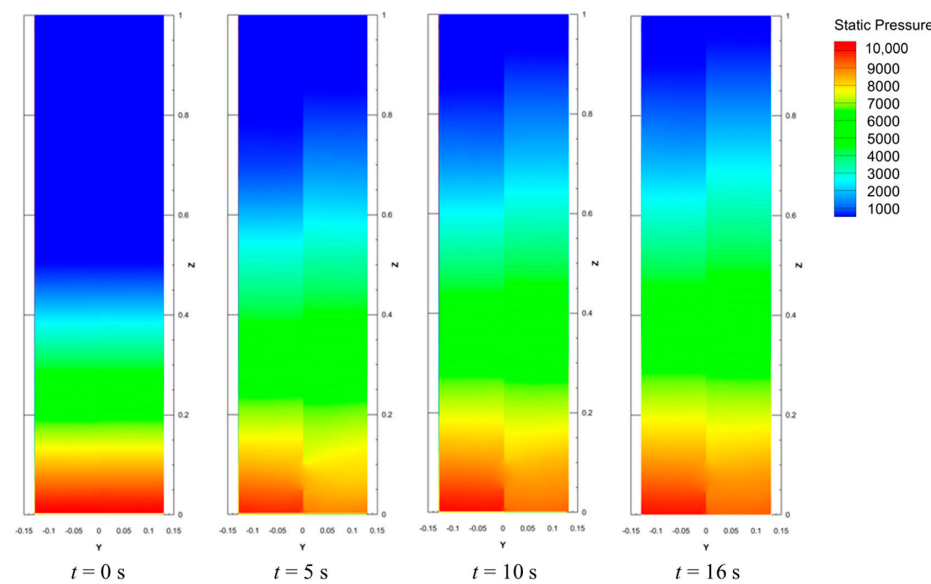


Figure 8. Instantaneous pressure profiles in IR-QFBP (plane $x = 0.075$ m).

4.3. Fluidization State

The fluidization state of the solid phase can be used as the indicator for achieving stable internal circulation. The instantaneous solid volume fractions in IR-QFBP with the inlet velocity of 0.1 m/s in high-speed beds and 0.06 m/s in low-speed beds are shown in Figure 9.

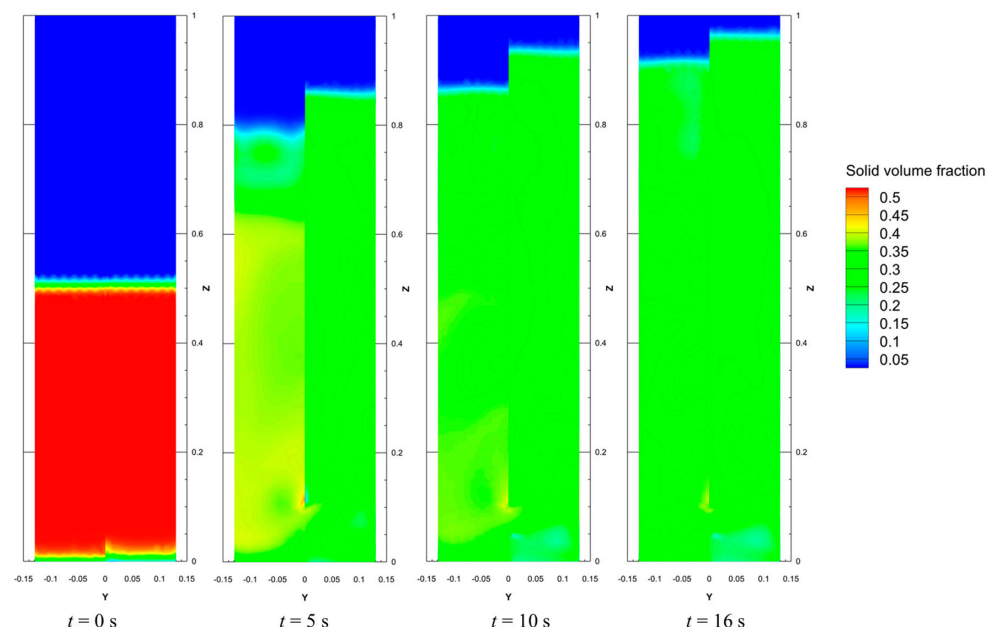


Figure 9. Instantaneous solid volume fractions in IR-QFBP (plane $x = 0.075$ m).

As shown in Figure 9, as time goes on, the bed heights of both high-speed bed and low-speed bed are growing. The expansion ratio of the bed begins to decrease at $t = 16$ s, while the bed heights are almost unchanged at $t = 16$ s. The solid volume fraction in the low-speed bed is higher than that in the high-speed bed after $t = 5$ s, especially around the top part of the lower connection between the two beds. With the increase in bed height, the solid volume fractions of the two beds are decreased. When the flow is fully developed, i.e., at $t = 16$ s, the bed height of the high-speed bed is higher than that of the low-speed bed because of the higher pressure at the top of the high-speed bed as shown in Figure 8.

4.4. Velocity Profiles of Solid Phase

In order to examine the flow characteristics in IR-QFBP, the streamline and velocity profiles of solid phase are shown in Figure 10. It can be seen clearly in Figure 10 that the solid particles in the high-speed bed enter the low-speed bed from the connecting hole in the upper part of the high-speed bed, while the solid particles in the low-speed bed enter the high-speed bed from the connecting hole in the lower part of the low-speed bed, which shows that the internal recycling is achieved between the two beds. Moreover, there are several flow vortexes formed in the beds, which can enhance mass transfer between the gas phase and the solid phase [44,45].

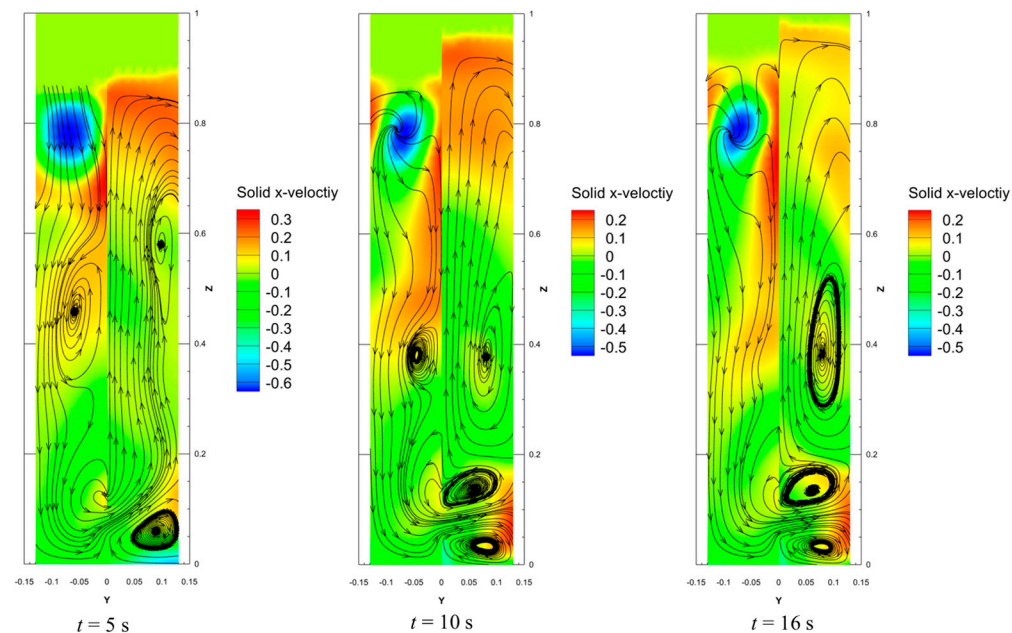


Figure 10. Streamline and velocity profiles of solid phase in IR-QFBP (plane $x = 0.075$ m).

4.5. Solid Circulation Rate

In this section, we investigated the solid circulation rate through the connection holes between the high-speed beds and low-speed beds, which can be used to measure the amount of the solid particle circulation and has a direct influence on the mean particle residence time [29]. The results of the solid particle circulation rates are shown in Table 5. Solid particle circulation rate through the lower connection is the same with that through the higher connection between the two beds. And, with the increase in the inlet velocity of low-speed bed, the solid particle circulation rates are increased. However, there is a small amount of the solid particles flowing out from the outlet of the high-speed bed (about 0.0002 kg/s) when the inlet velocity of the low-speed bed is 0.08 m/s, which can affect the subsequent process and increase the post-processing difficulty.

Table 5. Results of solid circulation rate through the connection hole.

	Inlet Velocity of High-Speed Bed (m/s)	Inlet Velocity of Low-Speed Bed (m/s)	Solid Circulation Rate through Lower Connection (kg/s)	Solid Circulation Rate through Higher Connection (kg/s)
Case 1	0.1	0.04	0.46	0.46
Case 2	0.1	0.06	0.62	0.62
Case 3	0.1	0.08	0.69	0.69

5. Conclusions

In this work, IR-QFBP, which can enable the coupling and heat transfer between different reactions, was proposed. It has potential for efficient reaction and energy utilization. The cold hydrodynamic characteristics of IR-QFBP, including the pressure profiles, fluidization states, velocity profiles, and circulation rates of the solid phase at different operation conditions were mainly investigated in this work. All the four cases (the cases with the inlet velocity of 0.1 m/s in high-speed beds and 0.04 m/s, 0.06 m/s, and 0.08 m/s in low-speed beds) focused on in the present work can achieve the stable internal circulation of solid materials. The case with the inlet velocity of 0.1 m/s in high-speed beds and 0.06 m/s in low-speed beds has the maximal solid circulating driving force. The case with the inlet velocity of 0.1 m/s in high-speed beds and 0.08 m/s can generate the highest solid circulation rate, but at the same time, they can give rise to a certain amount of solid material loss at the top outlet of IR-QFBP. Cold hydrodynamic characteristics' investigation of IR-QFBP in this work can provide the bases for modeling and designing of the corresponding hot reactor.

Author Contributions: X.C. conceived and designed the simulations; L.Z. and H.Y. analyzed the data; J.W. advised on the whole process of manuscript preparation; X.C. analyzed the data and wrote the paper. The analysis results and the paper were supervised by Y.H. All authors have read and agreed to the published version of the manuscript.

Funding: This research was funded by Natural Science Foundation of Hebei Province (grant number: B2022208045) and Youth Projects of National Natural Science Foundation of China (grant number: 22108060).

Data Availability Statement: Data are contained within the article.

Conflicts of Interest: The authors declare no conflicts of interest.

Nomenclature

Parameter

d_s	Particle diameter, m
e	Restitution coefficient
g	Gravitational acceleration (m/s^2)
g_0	Radial distribution function
I	Unit tensor
k_s	Conductivity of fluctuating energy, $\text{kg}/(\text{m}\cdot\text{s})$
p	Gas pressure, Pa
p_s	Solid pressure, Pa
u_f	Gas velocity, m/s
u_s	Solid velocity, m/s

Greek letters

α_f	Gas volume fraction
α_s	Solid volume fraction
β	Drag coefficient, $\text{kg}/(\text{m}^3\cdot\text{s})$

γ	Collisional dissipation of energy, $J/(m^3 \cdot s)$
θ_s	Granular temperature, m^2/s^2
λ_s	Solid phase bulk viscosity, $Pa \cdot s$
μ_f	Gas and solid viscosity, $Pa \cdot s$
μ_s	Solid viscosity, $Pa \cdot s$
$\mu_{s,col}$	Collisional part of solid viscosity, $Pa \cdot s$
$\mu_{s,kin}$	Kinetic part of solid viscosity, $Pa \cdot s$
$\mu_{s,fr}$	Frictional part of solid viscosity, $Pa \cdot s$
ρ_f	Gas density, kg/m^3
ρ_s	Solid density, kg/m^3
τ_f	Gas phase stress tensor, Pa
τ_s	Solid phase stress tensor, Pa

References

- Shi, X.; Wu, Y.; Zhang, J.; Ding, L.; Wang, C.; Lan, X.; Gao, J. Comparison of pyrolysis behavior between pure coal and mixture of coal/CaO. *J. Anal. Appl. Pyrolysis* **2021**, *159*, 105311. [[CrossRef](#)]
- Xue, F.; Li, D.; Guo, Y.; Liu, X.; Zhang, X.; Zhou, Q.; Ma, B. Technical Progress and the Prospect of Low-Rank Coal Pyrolysis in China. *Energy Technol.* **2017**, *5*, 1897–1907. [[CrossRef](#)]
- Wu, Y.; Shi, X.; Wang, C.; Gao, J.; Lan, X. CPFD Simulation of Hydrodynamics, Heat Transfer, and Reactions in a Downter Reactor for Coal Pyrolysis with Binary Particles. *Energy Fuels* **2019**, *33*, 12295–12307. [[CrossRef](#)]
- Shu, Z.; Fan, C.; Li, S.; Wang, J. Multifluid Modeling of Coal Pyrolysis in a Downter Reactor. *Ind. Eng. Chem. Res.* **2016**, *55*, 2634–2645. [[CrossRef](#)]
- Wu, L.; Guan, Y.; Li, C.; Shi, L.; Yang, S.; Reddy, B.R.; Ye, G.; Zhang, Q.; Liew, R.K.; Zhou, J.; et al. Free-radical behaviors of co-pyrolysis of low-rank coal and different solid hydrogen-rich donors: A critical review. *Chem. Eng. J.* **2023**, *474*, 145900. [[CrossRef](#)]
- Zhang, Y.; Zhao, Y.; He, X. Modeling coal pyrolysis in a cocurrent downter reactor. *Particuology* **2015**, *21*, 154–159. [[CrossRef](#)]
- Beis, S.; Onay, Ö.; Koçkar, Ö.M. Fixed-bed pyrolysis of safflower seed: Influence of pyrolysis parameters on product yields and compositions. *Renew. Energy* **2002**, *26*, 21–32. [[CrossRef](#)]
- Pütün, A.E.; Özbay, N.; Önal, E.P.; Pütün, E. Fixed-bed pyrolysis of cotton stalk for liquid and solid products. *Fuel Process Technol.* **2005**, *86*, 1207–1219. [[CrossRef](#)]
- Encinar, J.M.; González, J.F.; González, J. Fixed-bed pyrolysis of Cynara cardunculus L. Product yields and compositions. *Fuel Process Technol.* **2000**, *68*, 209–222. [[CrossRef](#)]
- Ly, H.V.; Kim, S.-S.; Woo, H.C.; Choi, J.H.; Suh, D.J.; Kim, J. Fast pyrolysis of macroalgae Saccharina japonica in a bubbling fluidized-bed reactor for bio-oil production. *Energy* **2015**, *93*, 1436–1446. [[CrossRef](#)]
- Xu, R.; Ferrante, L.; Briens, C.; Berruti, F. Flash pyrolysis of grape residues into biofuel in a bubbling fluid bed. *J. Anal. Appl. Pyrolysis* **2009**, *86*, 58–65. [[CrossRef](#)]
- Lee, S.-H.; Eom, M.-S.; Yoo, K.-S.; Kim, N.-C.; Jeon, J.-K.; Park, Y.-K.; Song, B.-H.; Lee, S.-H. The yields and composition of bio-oil produced from Quercus Acutissima in a bubbling fluidized bed pyrolyzer. *J. Anal. Appl. Pyrolysis* **2008**, *83*, 110–114. [[CrossRef](#)]
- Thomsen, T.P.; Sárossy, Z.; Gøbel, B.; Stoholm, P.; Ahrenfeldt, J.; Frandsen, F.J.; Henriksen, U.B. Low temperature circulating fluidized bed gasification and co-gasification of municipal sewage sludge. Part 1: Process performance and gas product characterization. *Waste Manag.* **2017**, *66*, 123–133. [[CrossRef](#)]
- Zuo, W.; Jin, B.; Huang, Y.; Sun, Y.; Li, R.; Jia, J. Pyrolysis of high-ash sewage sludge in a circulating fluidized bed reactor for production of liquids rich in heterocyclic nitrogenated compounds. *Bioresour. Technol.* **2013**, *127*, 44–48. [[CrossRef](#)]
- Lappas, A.A.; Samolada, M.C.; Iatridis, D.K.; Voutetakis, S.S.; Vasalos, I.A. Biomass pyrolysis in a circulating fluid bed reactor for the production of fuels and chemicals. *Fuel* **2002**, *81*, 2087–2095. [[CrossRef](#)]
- Sun, S.; Tian, H.; Zhao, Y.; Sun, R.; Zhou, H. Experimental and numerical study of biomass flash pyrolysis in an entrained flow reactor. *Bioresour. Technol.* **2010**, *101*, 3678–3684. [[CrossRef](#)] [[PubMed](#)]
- Dupont, C.; Commandré, J.-M.; Gauthier, P.; Boissonnet, G.; Salvador, S.; Schweich, D. Biomass pyrolysis experiments in an analytical entrained flow reactor between 1073K and 1273K. *Fuel* **2008**, *87*, 1155–1164. [[CrossRef](#)]
- Van de Velden, M.; Baeyens, J.; Brems, A.; Janssens, B.; Dewil, R. Fundamentals, kinetics and endothermicity of the biomass pyrolysis reaction. *Renew. Energy* **2010**, *35*, 232–242. [[CrossRef](#)]
- Ullah, A.; Shabbir, M.B.; Umair, M.; Nadeem, M.; Xin, F. Eulerian CFD analysis of clustering gas-solid flows in fluidized bed pyrolysis reactors. *J. Anal. Appl. Pyrolysis* **2021**, *158*, 105261. [[CrossRef](#)]
- Abaimov, N.; Ryzhkov, A.; Dubinin, A.; Ding, L.; Tuponogov, V.; Alekseenko, S. Investigation into the operation of an auto-thermal two-section subbituminous coal fluidized bed gasifier. *Int. J. Coal Sci. Technol.* **2023**, *10*, 37. [[CrossRef](#)]
- Zhang, J.; Wu, R.; Zhang, G.; Yao, C.; Zhang, Y.; Wang, Y.; Xu, G. Recent Studies on Chemical Engineering Fundamentals for Fuel Pyrolysis and Gasification in Dual Fluidized Bed. *Ind. Eng. Chem. Res.* **2013**, *52*, 6283–6302. [[CrossRef](#)]

22. Zhu, Y.; Li, K.; Wang, Q.; Cen, J.; Fang, M.; Luo, Z. Low-rank coal pyrolysis polygeneration technology with semi-coke heat carrier based on the dual-fluidized bed to co-produce electricity, oil and chemical products: Process simulation and techno-economic evaluation. *Fuel Process Technol.* **2022**, *230*, 107217. [[CrossRef](#)]
23. Xie, J.; Zhong, W.; Shao, Y.; Zhou, G. Simulation of co-gasification of coal and wood in a dual fluidized bed system. *Adv. Powder Technol.* **2021**, *32*, 52–71. [[CrossRef](#)]
24. Yan, L.; Cao, Y.; Li, X.; He, B. Characterization of a dual fluidized bed gasifier with blended biomass/coal as feedstock. *Bioresour. Technol.* **2018**, *254*, 97–106. [[CrossRef](#)]
25. Han, Z.; Zeng, X.; Yao, C.; Wang, Y.; Xu, G. Comparison of Direct Combustion in a Circulating Fluidized Bed System and Decoupling Combustion in a Dual Fluidized Bed System for Distilled Spirit Lees. *Energy Fuels* **2016**, *30*, 1693–1700. [[CrossRef](#)]
26. Hejazi, B.; Grace, J.R.; Bi, X.; Mahecha-Botero, A. Kinetic Model of Steam Gasification of Biomass in a Dual Fluidized Bed Reactor: Comparison with Pilot-Plant Experimental Results. *Energy Fuels* **2017**, *31*, 12141–12155. [[CrossRef](#)]
27. Liu, J.; Zhu, Z.; Jiang, H.; Lu, Q.; Zhang, H. Gasification of Bituminous Coal in a Dual-Bed System at Different Air/Coal Ratios. *Energy Fuels* **2015**, *29*, 496–500. [[CrossRef](#)]
28. Zhang, Y.; Wang, Y.; Cai, L.; Yao, C.; Gao, S.; Li, C.-Z.; Xu, G. Dual bed pyrolysis gasification of coal: Process analysis and pilot test. *Fuel* **2013**, *112*, 624–634. [[CrossRef](#)]
29. Ren, J.; Wang, Z.; He, B.; Yan, L.; Wang, Z.; Ding, G.; Ying, Z. Hydrodynamic Characteristics in a Cold Flow Model of Quadruple Fluidized Bed Gasifier. *Ind. Eng. Chem. Res.* **2020**, *59*, 4775–4784. [[CrossRef](#)]
30. Yan, L.; Cao, Y.; Li, X.; He, B. On a carbon-negative energy production scheme via a quadruple fluidized bed gasifier. *Energy Convers. Manag.* **2018**, *171*, 326–338. [[CrossRef](#)]
31. Yan, L.; He, B. On a clean power generation system with the co-gasification of biomass and coal in a quadruple fluidized bed gasifier. *Bioresour. Technol.* **2017**, *235*, 113–121. [[CrossRef](#)]
32. Yan, L.; Jia, Z.; Wang, Z.; He, B.; Fang, B. Numerical Research on Biomass Gasification in a Quadruple Fluidized Bed Gasifier. *Processes* **2022**, *10*, 2526. [[CrossRef](#)]
33. Abaimov, N.; Ryzhkov, A.; Tuponogov, V.; Simbiriatin, L.; Dubinin, A.; Ding, L.; Alekseenko, S. Steam Gasification in a Fluidized Bed with Various Methods of In-Core Coal Treatment. *Axioms* **2023**, *12*, 587. [[CrossRef](#)]
34. Yu, Z.; Chen, Y.; Feng, D.; Qian, Y. Process Development, Simulation, and Industrial Implementation of a New Coal-Gasification Wastewater Treatment Installation for Phenol and Ammonia Removal. *Ind. Eng. Chem. Res.* **2010**, *49*, 2874–2881. [[CrossRef](#)]
35. Feng, D.; Yu, Z.; Chen, Y.; Qian, Y. Novel Single Stripper with Side-Draw to Remove Ammonia and Sour Gas Simultaneously for Coal-Gasification Wastewater Treatment and the Industrial Implementation. *Ind. Eng. Chem. Res.* **2009**, *48*, 5816–5823. [[CrossRef](#)]
36. Shi, J.; Wang, N.; Li, L.; Li, Z.; Han, H. Review on treatment technologies of coal gasification wastewater in China. *J. Clean. Prod.* **2022**, *333*, 130166. [[CrossRef](#)]
37. Yuan, Y.; Li, D.; Zhang, L.; Zhu, Y.; Wang, L.; Li, W. Development, Status, and Prospects of Coal Tar Hydrogenation Technology. *Energy Technol.* **2016**, *4*, 1338–1348. [[CrossRef](#)]
38. LaMarche, C.Q.; Freireich, B.; Cocco, R.; Chew, J.W. Understanding drag part 1: Well-established drag limits and homogeneous drag laws. *Chem. Eng. J.* **2023**, *471*, 144541. [[CrossRef](#)]
39. Nijssen, T.M.J.; Padding, J.T.; Ottens, M. Hydrodynamics of expanded bed adsorption studied through CFD-DEM. *Chem. Eng. Sci.* **2023**, *280*, 119027. [[CrossRef](#)]
40. Wu, W.; Leckner, B.; Pallarès, D.; Duan, L. Solids separation efficiency at the outlet of a circulating fluidized bed riser. *Powder Technol.* **2023**, *428*, 118748. [[CrossRef](#)]
41. Kunii, D.; Levenspiel, O. *Fluidization Engineering*; Butterworth-Heinemann: Oxford, UK, 1991.
42. Gidaspow, D. Multiphase Flow and Fluidization: Continuum and Kinetic Theory Description. *J. Non-Newton Fluid.* **1994**, *55*, 207–208.
43. Liu, X.; Su, J.; Qian, Y.; Cui, L.; Liu, X. Comparison of two-fluid and discrete particle modeling of gas-particle flows in micro fluidized beds. *Powder Technol.* **2018**, *338*, 79–86. [[CrossRef](#)]
44. Dai, F.; Zhang, S.; Luo, Y.; Wang, K.; Liu, Y.; Ji, X. Recent Progress on Hydrogen-Rich Syngas Production from Coal Gasification. *Processes* **2023**, *11*, 1765. [[CrossRef](#)]
45. Gai, H.; Yang, P.; Zhang, Q.; Lin, M.; Song, H.; Xiao, M.; Huang, T.; Zhu, Q. Dual-dense gas-solid circulating fluidized bed reactor. *Fuel* **2023**, *337*, 126872. [[CrossRef](#)]

Disclaimer/Publisher’s Note: The statements, opinions and data contained in all publications are solely those of the individual author(s) and contributor(s) and not of MDPI and/or the editor(s). MDPI and/or the editor(s) disclaim responsibility for any injury to people or property resulting from any ideas, methods, instructions or products referred to in the content.